J. Microbiol. Biotechnol. (2015), 25(8), 1371–1379
http://dx.doi.org/10.4014/jmb.1501.01066

jmb

Asn-Linked Glycosylation Contributes to Surface Expression and Voltage-Dependent Gating of $Ca_v1.2$ Ca^{2+} Channel S

Hyun-Jee Park, Se-Hong Min, Yu-Jin Won, and Jung-Ha Lee*

Department of Life Science, Sogang University, Seoul 121-742, Republic of Korea

Received: January 23, 2015
Revised: March 25, 2015
Accepted: March 27, 2015

First published online
March 31, 2015

**Corresponding author*
Phone: +82-2-705-8791;
Fax: +82-2-704-3601;
E-mail: jhleem@sogang.ac.kr

Supplementary data for this paper are available on-line only at http://jmb.or.kr.

pISSN 1017-7825, eISSN 1738-8872

The $Ca_v1.2$ Ca^{2+} channel is essential for cardiac and smooth muscle contractility and many physiological functions. We mutated single, double, and quadruple sites of the four potential Asn (N)-glycosylation sites in the rabbit $Ca_v1.2$ into Gln (Q) to explore the effects of N-glycosylation. When a single mutant (N124Q, N299Q, N1359Q, or N1410Q) or $Ca_v1.2$/WT was expressed in *Xenopus* oocytes, the biophysical properties of single mutants were not significantly different from $Ca_v1.2$/WT. In comparison, the double mutant N124,299Q showed a positive shift in voltage-dependent gating. Furthermore, the quadruple mutant (QM; N124,299,1359,1410Q) showed a positive shift in voltage-dependent gating as well as a reduction of current. We tagged EGFP to the QM, double mutants, and $Ca_v1.2$/WT to chase the mechanisms underlying the reduced currents of QM. The surface fluorescence intensity of QM was weaker than that of $Ca_v1.2$/WT, suggesting that the reduced current of QM arises from its lower surface expression than $Ca_v1.2$/WT. Tunicamycin treatment of oocytes expressing $Ca_v1.2$/WT mimicked the effects of the quadruple mutations. These findings suggest that N-glycosylation contributes to the surface expression and voltage-dependent gating of $Ca_v1.2$.

Keywords: N-glycosylation, $Ca_v1.2$ Ca^{2+} channel, point mutation, *Xenopus* oocyte, voltage clamping

Introduction

Voltage-activated Ca^{2+} channels (VACCs) are hetero-multimeric membrane proteins composed of a pore-forming alpha1 (α_1) subunit and its auxiliary subunits ($\alpha_2\delta$, β, and γ). The largest α_1 subunits act as voltage-sensing and pore-forming machinery controlling external Ca^{2+} influx, mainly determining biophysical and pharmacological characteristics of VACCs, while the auxiliary subunits modulate the expression, drug binding sensitivity, and current kinetics of α_1 subunits [2, 12]. Molecular cloning and expression experiments have identified 10 α_1 subunit genes for VACCs of which functional types are assigned as follows. L-type Ca^{2+} channels are encoded by four Ca_v1 isoforms ($Ca_v1.1$–1.4). Non-L-type Ca^{2+} channels (N-, P/Q-, and R-type channels) are encoded by Ca_v2 ($Ca_v2.1$–2.3), respectively. Low voltage-activated T-type Ca^{2+} channels are encoded by three Ca_v3 isoforms ($Ca_v3.1$–3.3) [2, 12].

$Ca_v1.2$ is a member of the L-type Ca^{2+} subfamily ($Ca_v1.1$–1.4), which is predominantly expressed in heart and blood vessels. Electrical stimulation activates L-type $Ca_v1.2$ channel complex formed with auxiliary subunits, through which external Ca^{2+} entry induces Ca^{2+} release from ryanodine receptors in cardiac myocytes and activates calmodulin in smooth muscle, consequently signaling cascades leading to muscle contraction of heart and blood vessels. Additionally, expression of $Ca_v1.2$ was broadly detected in neuronal tissues, endocrine tissues, lung, trachea, and ovary, having suggested its functional implications in neuronal excitability, hormone secretion, activation of enzymes, and gene expression [7, 17]. The broad involvement of $Ca_v1.2$ in important physiological functions was supported by the identification of a missense mutation (G406R) of human $Ca_v1.2$, which is linked with Timothy syndrome, showing diverse dysfunctions in multi-organs, including cardiac arrhythmia, immune deficiency, hypoglycemia, abnormal cognition, and autism [15].

Ion channels in the plasma membrane have been reported

to be profoundly modified after translation by multiple types of post-translational processes, including glycosylation, formation of disulfide bond(s), enzyme digestion, phosphorylation(s), and ubiquitination. Asparagine (Asn, N)-linked glycosylation (N-glycosylation) has been reported to potently affect the structural folding, membrane targeting, expression level, stability, and voltage-dependent properties of many ion channels in the plasma membrane [14]. In $K_v1.5$, for example, removal of the N-glycosylation site by mutagenesis or lessening of N-glycans caused to positively shift voltage-dependency for channel gating [13]. Modification of N-glycosylation was reported to alter the activation and inactivation kinetics of $K_v3.1$ currents [6]. In TRESK and $K_v1.2$, N-glycosylation of the channels was shown to affect channel expression in the plasma membrane [3, 5]. Similarly, reduction or elimination of N-glycosylation of the $Ca_v3.2$ T-type Ca^{2+} channel was reported to decrease channel activity and expression with altered current kinetics [11, 16]. Furthermore, Orestes *et al*. [11] further suggested that deglycosylation treatments of $Ca_v3.2$ can be a potential method to relieve pain from diabetic peripheral neuropathy *via* a decrease of $Ca_v3.2$ channel activity.

In this study, we analyzed the amino acid sequence of the rabbit $Ca_v1.2$ α_1 subunit and found four potential sites for N-glycosylation (corresponding to "Asn-X-Thr/Ser") on the extracellular loops of the rabbit $Ca_v1.2$ subunit [9]. We examined functional roles of the N-glycosylation candidates by site-directed point mutations. Single point mutations of the four Asn residues did not cause any significant alterations, but the quadruple mutations of them caused to significantly reduce current amplitude, and to positively shift the voltage-dependent gating. These effects were mimicked by treatment of tunicamycin inhibiting N-glycosylation. These findings suggest that N-glycosylation plays critical roles in conferring its functional channel expression and biophysical properties to the $Ca_v1.2$ channel.

Materials and Methods

Chemicals

Most of the chemicals were purchased from Sigma–Aldrich (St. Louis, MO, USA). A PCR kit used to generate site-directed mutagenesis was purchased from Vivagen (Seoul, Korea).

Point Mutations of Potential N-Glycosylation Sites in $Ca_v1.2$

The rabbit $Ca_v1.2$ (GenBank Accession No. NM_001136522.1) contains four potential Asn-glycosylation sites: N124, N299, N1359, and N1410. The four Asn (N) sites were mutated into Gln (Q) using the PCR-based overlap extension method. Mutated site(s) were confirmed by sequencing analysis. The restriction enzyme sites were marked by numbers in parentheses. In total, seven mutants, including four single-site mutants, two double-site mutants, and one quadruple-site mutant, were generated.

N124Q. The forward primer to amplify the upper cassette for N124Q was AGCCATCGATGCGGCC and the reverse primer was AATTGGTGGCCTGGGAGTCATCTTCTGGAAAG. The forward primer to amplify the lower cassette for N124Q was AGA TGACTCCCAGGCCACCAATTCCAACCTG and the reverse primer was CATGAAGAGCTCCAGGCC. The upper and lower cassettes were connected by second-step PCR. N124Q was constructed by ligating the *Cla*I- and *Sac*I-digested PCR fragments into the *Cla*I- (448, $Ca_v1.2$) and *Sac*I-digested (1147, $Ca_v1.2$) plasmid $Ca_v1.2$ pGEM.

N299Q. The forward primer to amplify the upper cassette for N124Q was TTGCCAATTGTGTGGCCT and the reverse primer was ACACGGTGCCCTGCTGGCACTG CCGCCCG. The forward primer to amplify the lower cassette for N124Q was GCAGTG CCAGCAGGGCACCGTGTGCAAGCC and the reverse primer was TATTCCACCGGCGCCAG. The upper and lower cassettes were connected by second-step PCR. N124Q was constructed by ligating the *Mfe*I- and *Sfi*I-digested PCR fragments into the *Mfe*I- (689, $Ca_v1.2$) and *Sfi*I-digested (1759, $Ca_v1.2$) plasmid $Ca_v1.2$ pGEM.

N1359Q and N1410Q. The forward primer to amplify the upper cassettes for N1359Q and N1410Q was AAAGCACGTGGTTCA GTG and the reverse primers were CCGTGGTGTCCTGCAGGG CGATTTTCCCAAA and CTTCTGTGCTCTGGTGGGGCTCAG ACTCTG, respectively. The forward primers to amplify the lower cassettes for N1359Q and N1410Q were AATCGCCCTGCAGGA CACCACGGAGATCAAC and TGAGCCCCACCAGAGCAC AGAAGGGGAGACC, respectively, and the reverse primer was TTGCAAGCCACACGGTGA. The upper and lower cassettes were connected by second-step PCR. N1359Q and N1410Q were constructed by ligating the *Bsr*GI- and *Dra*III-PCR digested fragments, *Mfe*I (689, $Ca_v1.2$)-*Afl*II (2880, $Ca_v1.2$) fragment, and *Afl*II (2880, $Ca_v1.2$)-*Bsr*GI (3445, $Ca_v1.2$) fragment into the *Mfe*I- (689, $Ca_v1.2$) and *Dra*III-digested (4892, $Ca_v1.2$) plasmid $Ca_v1.2$ pGEM.

N124,299Q. N124,299Q was constructed by ligating the *Sac*I (1147, N299Q)-*Xma*I (6590, N299Q) fragment into the *Sac*I- (1147, N124Q) and *Xma*I-digested (6590, N124Q) plasmid N124Q pGEM.

N1359,1410Q. N1359,1410Q was constructed by introducing the N1410Q mutation into N1359Q. The upper and lower cassettes were obtained from N1359Q by PCR amplification using the same primer sets used to construct N1410Q. The upper and lower cassettes were combined by second-step PCR. N1359,1410Q was finally constructed by ligating the *Bsr*GI- and *Dra*III-digested PCR fragment, *Mfe*I (689, $Ca_v1.2$)-*Afl*II (2880, $Ca_v1.2$) fragment, and *Afl*II (2880, $Ca_v1.2$)-*Bsr*GI (3445, $Ca_v1.2$) fragment into the *Mfe*I- (689, $Ca_v1.2$) and *Dra*III-digested (4892, $Ca_v1.2$) plasmid $Ca_v1.2$ pGEM.

N124,299,1359,1410Q (quadruple mutant; QM). The quadruple mutant was constructed by ligating the *Mfe*I (689, N124,299Q)-*Afl*II (2880, N124,299Q) fragment into the *Mfe*I- (689) and *Sac*I-digested (1147) plasmid N1359,1410Q pGEM.

Expression of $Ca_v1.2$ and Mutant Channels in *Xenopus* Oocytes

The GenBank accession numbers of rabbit $Ca_v1.2$ and rat β_3 are NM_001136522.1 and M88751, respectively. *In vitro* synthesis of cRNAs and their expression in *Xenopus* oocytes were reported previously [8]. Briefly, the $Ca_v1.2$ and mutant cDNAs were linearized at their 3′ ends by *Hin*dIII, while the β_3 cDNA was linearized by *Sac*II. cRNA transcripts were *in vitro* synthesized using T7 RNA polymerase (Ambion, Austin, TX, USA). Female *Xenopus laevis* frogs were obtained from Hallym University (Gangwon-do, Chuncheon, Korea). Several ovary lobes were surgically cut from frogs under anesthesia and manually torn into small clusters of 4–6 eggs in a standard oocyte solution (SOS; in mM: 100 NaCl, 2 KCl, 1.8 $CaCl_2$, 1 $MgCl_2$, 5 HEPES, 2.5 pyruvic acid, and 50 μg/ml gentamicin; pH 7.6). Follicle membranes were eliminated by shaking the oocyte clusters treated with collagenase (10 mg/ml; Gibco-BRL, Gaithersburg, MD, USA) in a Ca^{2+}-free solution (in mM: 82.5 NaCl, 2.5 KCl, 1 $MgCl_2$, and 5 HEPES; pH 7.6) for 40–60 min. Each oocyte was injected with ~5 ng of α_1 subunit cRNA and 2.5 ng of β_3 cRNA in a volume of 50 nl using a Drummond Nanoject pipette injector (Parkway, PA, USA) attached to a Narishige micromanipulator (Tokyo, Japan) under a stereo microscope.

Electrophysiological Recordings in Oocytes and Data Analysis

Recording of Ba^{2+} currents from oocytes were performed between 3 and 5 days after cRNA injection at room temperature by a two-electrode voltage clamping method, for which a two-electrode voltage-clamp amplifier (OC-725C; Warner Instruments, Hamden, CT, USA) was utilized. Glass microelectrodes were pulled from capillaries (Warner Instruments, Hamden, CT, USA) using a pipette puller (P97; Sutter Instrument Co., Novato, CA, USA), and filled with 3 M KCl, and the electrode resistance was ~1.0 MΩ. The recording solution contained 10 mM $Ba(OH)_2$, 90 mM NaOH, 1 mM KOH, and 5 mM HEPES (pH 7.4 adjusted with methanesulfonic acid). The currents were sampled at 5 kHz and low pass-filtered at 1 kHz using the pClamp system (Digidata 1322A and pClamp 8; Molecular Devices, Palo Alto, CA, USA). Properties of the currents were analyzed using Clampfit software (Axon Instruments).

Activation curves were generated by the chord conductance method, in which the cord conductance (G) was calculated by dividing the current amplitude by the driving force (reversal potential–test potentials), and normalized to the maximum conductance. Activation curves were from fitting the normalized data to the Boltzmann equation ($G = 1/[1+\exp(V_{50,act}-V)/k]$, where $V_{50,act}$ is the half-activation voltage, and k is the slope factor). The protocol for steady-state inactivation consisted of 10 sec prepulses between -90 mV and +30 mV from a holding potential of -80 mV, followed by a test potential of +10 mV. Peak currents were calculated to ratios to the maximal current elicited after a 10 sec prepulse potential of -90 mV and the ratios were plotted against prepulse potentials. The curve for steady-state inactivation was from fitting the data points with a Boltzmann equation ($1/[1+\exp(V_{50,inact}-V)/k]$, where $V_{50,inact}$ is the potential for half-inactivation and k is the slope factor).

Graphical representation of the data was achieved with Prism software (GraphPad, San Diego, CA, USA). Data are given as the mean ± SEM. Differences were tested for significance using Student's unpaired *t* tests and one-way ANOVA Tukey tests, with $p < 0.05$ as the level of significance.

Results

Potential N-Glycosylation Sites in Rabbit $Ca_v1.2$

The amino acid sequence of the rabbit $Ca_v1.2$ α_1 subunit (GenBank No. NM_001136522.1) was analyzed to look for the potential N-glycosylation motif (Asn-X-Thr/Ser) in its extracellular loops, in which the 1st Asn (N) residue is separated from the 3rd Ser or Thr residue by an amino acid (X), which can be all the amino acid residues except Pro. The rabbit $Ca_v1.2$ contains four potential N-glycosylation sites (N124, N299, N1359, and N1410), which are marked on the schematic diagram of the rabbit $Ca_v1.2$ (Fig. 1). N124 and N299 are positioned in the S1-S2 and S5-S6 linkers in domain I of the $Ca_v1.2$. Both N1359 and N1410 are positioned in the S5-S6 linker in domain IV.

Single Site Mutations Did Not Alter Biophysical Properties of the $Ca_v1.2$

We first performed experiments to confirm the expression of $Ca_v1.2$ L-type channels in the oocyte system using nifedipine, which is known to be an L-type Ca^{2+} channel antagonist. Ba^{2+} currents from oocytes expressing $Ca_v1.2$ channels were evoked by +10 mV step pulses from a holding potential of -80 mV. Application of 1 μM nifedipine potently inhibited $Ca_v1.2$ currents, and the average inhibition percentage was about 80% (Fig. S1). This nifedipine-sensitive blockade supports that the $Ca_v1.2$ L-type channels were expressed in oocytes.

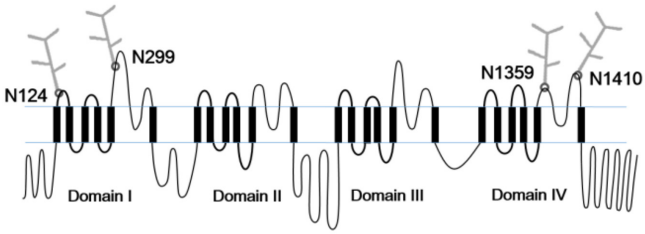

Fig. 1. Potential N-glycosylation sites in rabbit $Ca_v1.2$.
The schematic diagram of the rabbit $Ca_v1.2$ α_1 subunit (GenBank # NM_001136522.1) exhibits the locations of four potential N-glycosylation sites in the extracellular surface: N124, N299, N1359, and N1410. N124 and N299 are in domain I of the $Ca_v1.2$, and N1359 and N1410 are in domain IV.

To examine individual functions of the four potential N-glycosylation sites, we generated N124Q, N299Q, N1359Q, and N1410Q by mutating each of the four Asn (N) residues into Gln (Q). An equal amount (5 ng) of $Ca_v1.2$/WT cRNA or single-site mutant cRNA was co-injected with β_3 cRNA (2.5 ng) into *Xenopus* oocytes. Their expression was detected as robust inward currents from the oocytes from the 3rd day after cRNA injection. Their representative current traces elicited by serial step pulses to -40, -10, +10, and +30 mV from a holding potential of -80 mV are displayed (Figs. 2A–2E). Their average current-voltage (I-V) data appeared to be almost overlapped (Fig. 2F), suggesting that the relevant properties of the single-site mutants are similar to those of $Ca_v1.2$/WT, including average current amplitude at various test potentials, voltage-dependency for activation, and reversal potential. When their cord conductance data derived from I-V data were plotted and analyzed (Fig. 2G), the $V_{50,act}$ values (50% activation potential) for $Ca_v1.2$/WT, N124Q, N299Q, N1359Q, and N1410Q were -7.2 ± 0.7, -8.4 ± 0.8, -7.5 ± 0.8, -7.7 ± 0.8, and -6.8 ± 0.7 mV, and their slope factors were 6.2 ± 0.4, 6.4 ± 0.5, 6.1 ± 0.5, 6.2 ± 0.5, and 6.7 ± 0.3 mV, respectively. The $V_{50,act}$ values and slope factors were not significantly different among them (one-way ANOVA Tukey tests, $n = 9–14$). Analysis of steady-state inactivation data showed that the $V_{50,inact}$ values for $Ca_v1.2$/WT, N124Q, N299Q, N1359Q, and N1410Q were -17.7 ± 0.7, -18.0 ± 0.6, -17.7 ± 0.9, -19.5 ± 0.7, and -18.7 ± 0.6 mV, and their slope factors were -10.5 ± 0.6, -9.8 ± 0.5, -11.2 ± 0.8, -11.3 ± 0.7, and -10.1 ± 0.5 mV, respectively (Fig. 2H). The $V_{50,inact}$ values and slope factors were not significantly different among the groups (one-way ANOVA Tukey tests, $n = 7–9$). These results strongly suggest that disruption of

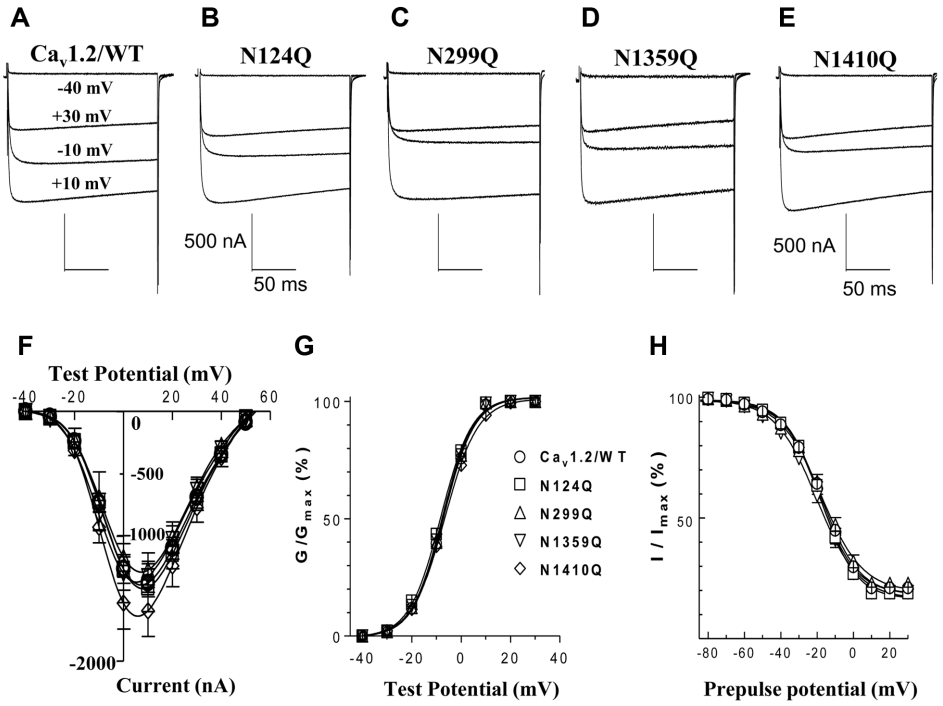

Fig. 2. Electrophysiological properties of single N-glycosylation site mutants.

(**A**–**E**) Representative current traces through $Ca_v1.2$/WT (**A**), N124Q (**B**), N299Q (**C**), N1359Q (**D**), and N1410Q (**E**). In an extracellular 10 mM Ba^{2+} solution, current traces were elicited from oocytes expressing $Ca_v1.2$/WT or each single mutant with β_3 by a voltage protocol composed of depolarizing step pulses in 10 mV increments, from a holding potential of -80 mV. Among them, current traces evoked by step pulses to -40, -10, +10, and +30 mV from a holding potential of -80 mV are shown. (**F**) Average current-voltage (I-V) relationships of $Ca_v1.2$/WT (○), N124Q (□), N299Q (△), N1359Q (▽), and N1410Q (◇). Averaged current values (± SEM) were plotted against test potentials. Significant differences between average currents of $Ca_v1.2$/WT and the single mutants were not detected over most of test potentials (one-way ANOVA Tukey tests, $p > 0.05$, $n = 9$-14). (**G**) Activation curves of $Ca_v1.2$/WT and single mutants. Activation curves were generated by the chord conductance method (refer to the Methods section). The $V_{50,act}$ values and slope factors for $Ca_v1.2$/WT and the single mutants are not different among them (one-way ANOVA Tukey tests, $p > 0.05$, $n = 9–14$). (**H**) Steady-state inactivation curves of $Ca_v1.2$/WT and single mutants. The inactivation protocol and generation of steady-state inactivation curves are described in the Methods section. The $V_{50,iact}$ values and slope factors for $Ca_v1.2$/WT and the single mutants were not different among them (one-way ANOVA Tukey tests, $p > 0.05$, $n = 7–9$).

any single site among the four potential N-glycosylation sites does not significantly affect the biophysical properties, including current amplitude and voltage-dependency for activation and steady-state inactivation.

Quadruple Mutation for N-Glycosylation Sites Altered the Biophysical Properties of $Ca_v1.2$

We additionally generated double-site mutants (N124,299Q and N1359,1410Q) and a quadruple-site mutant (N124,299,1359,1410Q) to examine whether these mutations of the N-glycosylation sites have effects on channel expression and biophysical properties. When an equal amount (5 ng) of each cRNA for $Ca_v1.2$/WT, the double mutants, and QM was coinjected with β_3 cRNA (2.5 ng) into oocytes, strong inward currents were recorded from the oocytes from the 3rd day after cRNA injection (Figs. 3A–3D). Ba^{2+} currents of the double mutants (N124,299Q and N1359,1410Q) evoked by the I-V protocol were not significantly different from $Ca_v1.2$/WT currents in amplitude, whereas Ba^{2+} currents of QM (N124,299,1359,1410Q) were significantly smaller than $Ca_v1.2$/WT currents (Figs. 3A–3E; one-way ANOVA Tukey tests, $p < 0.05$, $n = 9–14$).

When the I-V data of the double and quadruple mutants were normalized to that of $Ca_v1.2$/WT for comparison

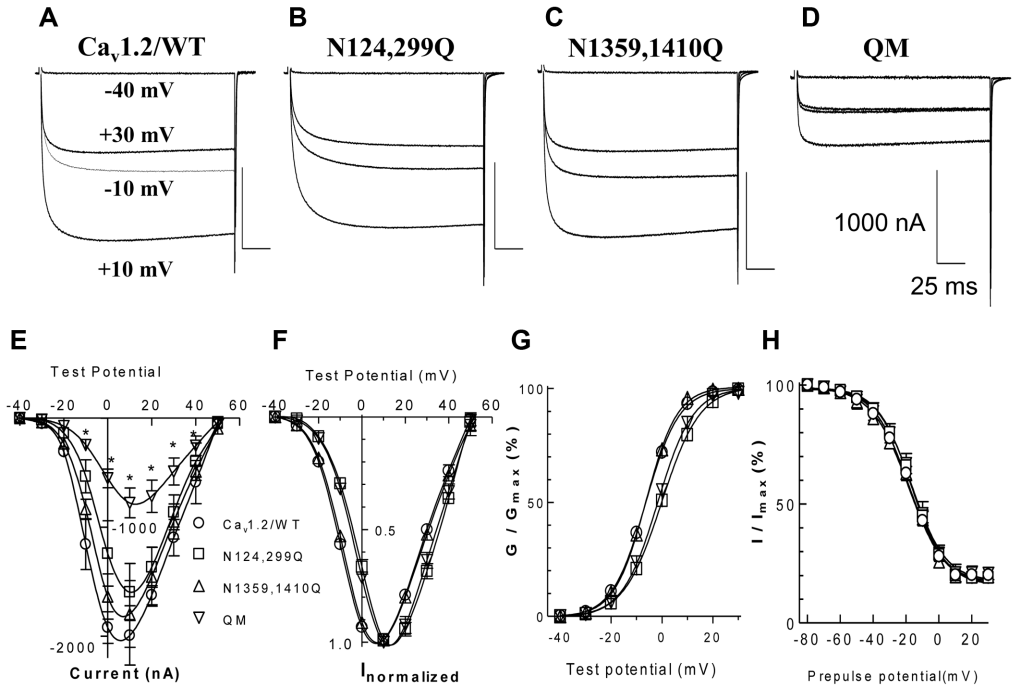

Fig. 3. Current traces and I-V relationships of the double and quadruple mutants.

(**A–D**) Representative current traces of $Ca_v1.2$/WT (control), and double and quadruple mutant channels. In 10 mM Ba^{2+} solution, currents were evoked by a voltage protocol composed of serial voltage steps ranging from -40 mV to +60 mV by 10 mV increments, from a holding potential of -80 mV. Superposed current traces of $Ca_v1.2$/WT (**A**), N124,299Q (**B**), N1359,1410Q (**C**), and QM (**D**) elicited by test potentials of -40, -10, +10, and +30 mV from a holding potential of -80 mV are represented. (**E**) Current-voltage (I-V) relationships of the $Ca_v1.2$/WT, double mutants, and QM. The average current amplitudes of $Ca_v1.2$/WT (○, $n = 14$), N124,299Q (□, $n = 9$), N1359,1410Q (△, $n = 9$), and QM (△, $n = 9$) were plotted against test potentials, as described in Fig. 2F. Statistical differences are indicated with asterisks (*, $p < 0.05$, one-way ANOVA Tukey tests, n = 9–14). (**F**) Normalized current-voltage (I-V) relationships of double and quadruple mutants and $Ca_v1.2$/WT. Current amplitudes of $Ca_v1.2$/WT, N124,299Q, N1359,1410Q, or QM elicited by a voltage protocol were normalized to the maximal current amplitude observed and then normalized average values were plotted against test potentials. (**G**) Activation curves of $Ca_v1.2$/WT, double mutants, and QM. Activation curves were derived from fitting cord conductance (G) as explained in the Methods section. The $V_{50,act}$ values (50% activation potential) and slope factors (k) for $Ca_v1.2$/WT, N124,299Q, N1359,1410Q, and QM were estimated from the fittings using the Boltzmann equation. The $V_{50,act}$ values for N124,299Q and QM a significantly different from those of $Ca_v1.2$/WT and N1359,1410Q (one-way ANOVA Tukey tests, $p < 0.05$, $n = 9–14$). (**H**) Steady-state inactivation curves of $Ca_v1.2$/WT, double mutants, and QM. The $V_{50,inact}$ values for $Ca_v1.2$/WT, N124,299Q, N1359,1410Q, and QM were estimated to be -18.4 ± 0.9, -16.8 ± 0.9, -18.5 ± 1.1, and -17.0 ± 0.9 and their slope factors (k) were -10.5 ± 0.7, -10.2 ± 0.6, -11.3 ± 1.1, and -10.4 ± 0.9, respectively. Significant differences were not detected among them (one-way ANOVA Tukey tests, $n = 8–12$).

(Figs. 3E and 3F), the I-V relationships of N124,299Q and QM were shown to be positively shifted, compared with that of $Ca_v1.2$/WT. Their activation curves were from fitting their cord conductance(s) calculated from the I-V data (Fig. 3G). The $V_{50,act}$ values for $Ca_v1.2$/WT, N124,299Q, N1359,1410Q, and QM were -6.45 ± 0.15, -0.98 ± 0.13, -6.18 ± 0.52, and -0.91 ± 0.24 mV, respectively. Statistical analysis showed that the $V_{50,act}$ values for N124,299Q and QM were significantly different from that of $Ca_v1.2$/WT (one-way ANOVA Tukey tests, $p < 0.05$), but their slope factors were not significantly different from $Ca_v1.2$/WT. This finding consistently suggests that the activation curves of N124,299Q and QM were significantly shifted to the depolarizing direction. In comparison, the double mutations in domain IV did not cause any significant alterations in current amplitude and voltage-dependent gating.

The steady-state inactivation curves of $Ca_v1.2$/WT, N124,299Q, N1359,1410Q, and QM were obtained from fitting the data to the Boltzmann equation (Fig. 3H). The $V_{50,inact}$ values and slope factors for $Ca_v1.2$/WT, N124,299Q, N1359,1410Q, and QM were not significantly different, suggesting that the voltage dependency for steady-state inactivation was not significantly altered by the double or quadruple mutations.

Taken together, electrophysiological characterizations of the mutant channels indicate that the single-site mutations did not significantly alter the biophysical properties of $Ca_v1.2$, but the double mutation in domain I caused a positive shift of the activation curve. Moreover, the quadruple mutation caused a positive shift of the activation curve and a decrease of current.

Less Surface Expression of EGFP-QM than EGFP-$Ca_v1.2$/WT

To explore the mechanism(s) underlying the reduced currents of QM compared with $Ca_v1.2$/WT and the double mutants, we engineered to tag EGFP cDNA to the 5′ end of $Ca_v1.2$/WT cDNA, N124,299Q cDNA, N1359,1410Q cDNA, and QM cDNA. An equal amount (5 ng) of EGFP-$Ca_v1.2$/WT cRNA, EGFP-N124,299Q cRNA, EGFP-N1359,1410Q cRNA, or EGFP-QM cRNA was coinjected with β_3 cRNA (2.5 ng) into oocytes. Localization of EGFP-$Ca_v1.2$/WT, EGFP-N124,299Q, EGFP-N1359,1410Q, and EGFP-QM in the oocyte plasma membrane was observed *via* their fluorescence images under a confocal microscope on the 4th day after cRNA injection (Fig. 4A). Analysis of the fluorescence images at the oocyte membrane showed that the average fluorescence intensity for EGFP-QM was significantly weaker than those for EGFP-$Ca_v1.2$/WT, EGFP-N124,299Q, and EGFP-N1359,1410Q (Fig. 4B). These findings suggest

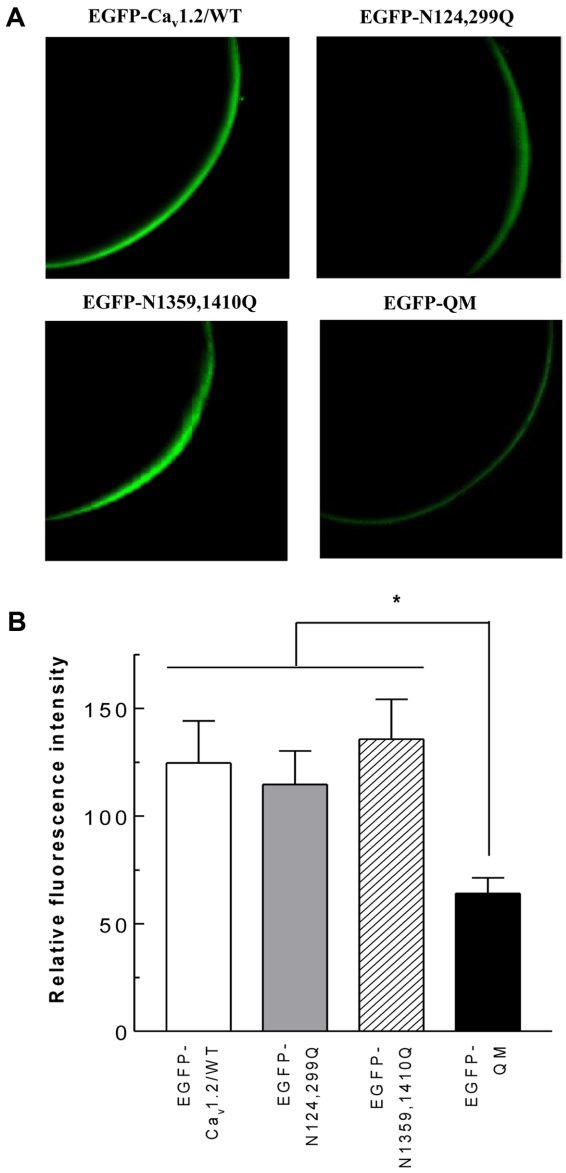

Fig. 4. Surface expression of EGFP-$Ca_v1.2$/WT, EGFP-double mutants, and EGFP-QM.

(**A**) Representative confocal images of fluorescence of oocytes expressing EGFP-$Ca_v1.2$/WT, EGFP-N124,299Q, EGFP-N1359,1410Q, or EGFP-QM. Surface fluorescence images were taken from oocytes injected with cRNA (5 ng) of EGFP-$Ca_v1.2$/WT, EGFP-N124,299Q, EGFP-N1359,1410Q, or EGFP-QM with β_3 cRNA (2.5 ng), using a Zeiss confocal microscope. (**B**) Relative fluorescent intensities of EGFP-tagged $Ca_v1.2$ constructs at the oocyte surface. The fluorescence intensities at the surface of oocytes expressing EGFP-$Ca_v1.2$/WT, EGFP-N124,299Q, EGFP-N1359,1410Q, or EGFP-QM were quantitated using the ImageJ program. Their average fluorescence values (arbitrary unit) were 124.6 ± 18.3, 114.6 ± 15.7, 135.6 ± 17.8, and 64.1 ± 7.1, respectively, which are represented in the bar graphs. Significant differences were detected between the fluorescence intensities of EGFP-QM and the other groups (one-way ANOVA Tukey tests, $p < 0.05$, $n = 8–10$).

that the smaller current of QM than the $Ca_v1.2$/WT and double-mutant channels may arise from the lower surface expression of QM than $Ca_v1.2$/WT.

Tunicamycin Treatment of $Ca_v1.2$/WT Mimics the Quadruple Mutation Effects

To examine whether treatment of tunicamycin, a specific inhibitor of N-linked glycoslylation *via* inhibiting N-acetylglucosamine transferase, can affect the biophysical properties of $Ca_v1.2$/WT, we prepared two sets of oocytes. A control set of oocytes were injected with only a cRNA mixture of $Ca_v1.2$/WT and β_3, whereas the other set of oocytes were coinjected with tunicamycin (3 ng/oocyte) and cRNA mixture of $Ca_v1.2$/WT and β_3. From 3–4 days after injection, we recorded currents from the two groups of oocytes. Analysis of I-V data (Fig. 5A) showed that the currents of the tunicamycin-treated group were significantly smaller than those of the control $Ca_v1.2$/WT group over most of the test potentials (Student's unpaired *t* tests, $p < 0.05$, n = 10-12), implying that the current reduction may be caused by disruption of N-glycosylation on $Ca_v1.2$/WT by the drug. In addition, the I-V of the tunicamycin-treated group seems to be positively shifted, compared with that of the control group (Fig. 5A). This positive shift of I-V curves was consistently detected in their activation curves (Fig. 5C). The $V_{50,act}$ values for the $Ca_v1.2$/WT and the tunicamycin-treated $Ca_v1.2$/WT were -6.4 ± 0.3 mV and -2.0 ± 0.4 mV, and their slopes were 6.7 ± 0.3 and 6.8 ± 0.3, respectively. The $V_{50,act}$ value for the tunicamycin-treated $Ca_v1.2$/WT was significantly bigger than that of the $Ca_v1.2$/WT, suggesting that tunicamycin positively shifted the activation curve of $Ca_v1.2$/WT.

Next experiments were performed to compare steady-state inactivation properties between the control $Ca_v1.2$/WT group and the tunicamycin-treated $Ca_v1.2$/WT. Analysis of their steady-state inactivation curves (Fig. 5D) showed that the $V_{50,inact}$ values of the control $Ca_v1.2$/WT group and the tunicamycin-treated $Ca_v1.2$/WT groups were -18.0 ± 0.9 and -16.8 ± 1.1, and their slope factors (k) were -10.7 ± 0.7 and -10.2 ± 0.6, respectively. Significant differences were not found between the relevant values of the two groups (Student's unpaired *t* tests). These results suggest that tunicamycin treatment mimics the effects caused by the quadruple mutations of potential N-glycosylation sites, supporting that N-glycosylation can significantly affect the surface expression and voltage-dependent gating of $Ca_v1.2$.

To elucidate the decrement effect on $Ca_v1.2$/WT currents by treatment of tunicamycin (Fig. 5A), we examined whether tunicamycin can affect the surface expression of

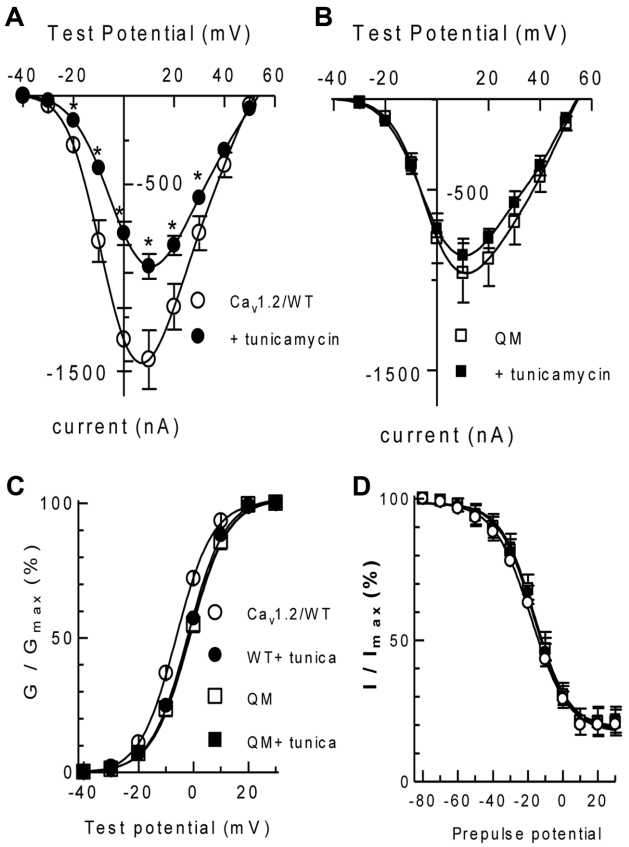

Fig. 5. Effects of tunicamycin on $Ca_v1.2$/WT and QM.
A control group of oocytes were injected with only a cRNA mixture of $Ca_v1.2$/WT (**A**) or QM (**B**) and β_3, whereas the other group of oocytes were injected with tunicamycin (3 ng/oocyte) as well as cRNA mixture of $Ca_v1.2$/WT or QM and β_3. (**A–B**) Effects of tunicamycin on the I-V curves of $Ca_v1.2$/WT and QM. Ba^{2+} currents through $Ca_v1.2$/WT and QM were elicited by the same voltage protocol used in Fig. 1. They were averaged and then plotted against test potentials. The symbols and sample numbers are as follows: $Ca_v1.2$/WT control (○, n = 12); tunicamycin-treated $Ca_v1.2$/WT (●, n = 10); QM control (□, n = 8); tunicamycin-treated QM (■, n = 7). Statistical differences were marked with asterisks (*, $p < 0.05$, Student's unpaired *t*-tests). (**C**) Activation curves of the control groups and the test groups treated with tunicamycin. Activation curves were obtained as described in the Methods section. Their $V_{50,act}$ values were significantly different (Student's unpaired *t* test, $p < 0.05$, n = 12, 10). The $V_{50,act}$ values for the QM control and the tunicamycin-treated QM were -1.5 ± 0.4 mV and -1.2 ± 0.4 mV and their slope factors 6.6 ± 0.4 and 6.9 ± 0.6, respectively. No significant difference was detected (Student's unpaired *t* test, $p > 0.1$, n = 8, 7). (**D**) Tunicamycin effects on the steady-state inactivation properties of $Ca_v1.2$/WT and QM. The $V_{50,inact}$ values for $Ca_v1.2$/WT, tunicamycin-treated $Ca_v1.2$/WT, QM, and tunicamycin-treated QM were -18.0 ± 0.9, -16.8 ± 1.1, -16.2 ± 1.0, and -16.3 ± 0.9 and their slope factors (k) were -10.7 ± 0.7, -10.2 ± 0.6, -11.3 ± 1.1, and -10.4 ± 0.9, respectively. Significant differences were not detected among the parameters (Student's unpaired *t* tests, n = 10–12).

EGFP-tagged $Ca_v1.2$/WT in oocytes. Analysis of fluorescence images in the membrane regions of oocytes showed that the average fluorescent intensity (117.6 ± 18.6) of the control group injected with the cRNA mixture (EGFP-$Ca_v1.2$/WT and β_3) was significantly greater than the intensity (70.6 ± 11) of the test group injected with the cRNA mixture plus tunicamycin (Fig. S2). The reduced fluorescence intensity of the tunicamycin group suggests that the drug might disrupt N-glycosylation of the channels, resulting in a significant decrease in the surface expression of EGFP-$Ca_v1.2$/WT. This may be a possible underlying mechanism for the reduction effects on $Ca_v1.2$/WT currents by tunicamycin.

We finally examined whether tunicamycin can alter the biophysical properties of QM. Analysis of the I-V data showed that tunicamycin did not alter the current amplitudes of QM over most of the test potentials (Fig. 5B). Analysis of the activation curves and the steady-state inactivation curves displayed that the drug did not significantly change the voltage dependency for activation and steady-state inactivation (Figs. 5C and 5D). These results suggest that tunicamycin did not affect the biophysical properties of QM in which potential N-glycosylation sites were abolished by site-directed mutagenesis.

Discussion

We here showed that single mutations of the potential N-glycosylation sites on $Ca_v1.2$ did not have significant effect(s) on the biophysical properties of $Ca_v1.2$. It is thus limited to specify function(s) of each of the four potential N-glycosylation sites. In comparison, double mutations of the two sites in domain I, but not in domain IV, caused a depolarizing shift in voltage-dependent gating. Furthermore, the quadruple mutation caused a strong reduction of current amplitude as well as a positive shift of voltage-dependent gating. Consistently, the tunicamycin treatment mimicked the biophysical effects led by the quadruple mutation, whereas it did not affect those of QM in which all the potential N-glycosylation sites were abolished by site-directed point mutations. Taken together, these findings suggest that N-glycosylation would contribute to the surface expression and voltage-dependent gating of $Ca_v1.2$/WT.

Our finding that disruption of the two N-glycosylation sites in domain I of the $Ca_v1.2$ induced a positive shift in voltage-dependent gating is consistent with the effects found in $Na_v1.4$ [1]. Negatively charged glycan(s) are attached to nitrogen atoms of Asn residues in N-linked glycosylation, potentially contributing to the creation of a negative potential on the extracellular surface. Because elimination of N-glycosylation can reduce the negative surface potential formed by the attachment of glycan(s), depolarized potential needs to be applied for channel gating to overcome the reduced negative surface potential. This may account for the depolarizing shifts in channel gating, which were detected in the quadruple mutant and the double mutant in domain I of $Ca_v1.2$.

Among the four potential N-glycosylation sites, three sites (N299, N1359, and N1410) are positioned at the pore loops (S5-S6) of domains I and IV (Fig. 1). Although single mutations of them were not sufficient to alter the functions of $Ca_v1.2$, we speculate that the three sites critically influence the voltage-dependent gating and/or the surface expression of $Ca_v1.2$ in a distinctive way. Serial construction and characterization of pore N-glycosylation mutants (N124,1359Q, N299,1410Q, and N124,1359,1410Q) remain to be further undertaken in the future, which may provide important information to unveil the underlying mechanisms for the functions of N-glycosylation.

Fluorescence imaging studies of EGFP-QM, EGFP-double mutants, and EGFP-$Ca_v1.2$/WT suggest that the reduced currents of EGFP-QM arise from its reduced surface expression probably *via* decreased membrane targeting of EGFP-QM proteins after translation, compared with the EGFP-$Ca_v1.2$/WT and EGFP-double mutants. However, it remains to further investigate the detailed mechanisms for the reduced surface expression, which might involve various steps as follows. First, we speculate that disruption of N-glycosylation sites on the $Ca_v1.2$ might negatively affect the structural folding of $Ca_v1.2$ proteins after protein synthesis. Second, improperly folded $Ca_v1.2$ proteins and/or N-glycosylation-deficient $Ca_v1.2$ proteins might be less efficiently targeted to the membrane as well. Third, improperly folded $Ca_v1.2$ proteins or N-glycosylation-deficient $Ca_v1.2$ proteins might be more labile for degradation.

The pathophysiological relevance of N-glycosylation-deficient $Ca_v1.2$ can be found in patients with congenital disorders of N-linked glycosylation (CDG) [4, 10]. The patients would have membrane proteins lacking of N-glycosylation. Considering that $Ca_v1.2$ channels are expressed in the cardiovascular system, endocrine system, nervous system, and diverse peripheral systems, CDG patients would be severely implicated in cardiovascular malfunctions and broad types of pathophysiological conditions in the other systems, because N-glycosylation deficiency in $Ca_v1.2$ would cause a reduction of current *via* reduced surface expression and a positive shift in voltage-dependent gating of $Ca_v1.2$. In conclusion, our combined approaches of site-

directed mutagenesis, electrophysiology, and confocal imaging studies support that N-glycosylation critically contributes to membrane trafficking for the functional expression and voltage-dependent gating of $Ca_v1.2$.

Acknowledgments

This work was supported by the Sogang University Special Research Grant 2014 (201410035) and the Priority Research Centers Program (2012-0006690) through the National Research Foundation of Korea to JH Lee.

References

1. Bennett ES. 2002. Isoform-specific effects of sialic acid on voltage-dependent Na^+ channel gating: functional sialic acids are localized to the S5-S6 loop of domain I. *J. Physiol.* **538:** 675-690.
2. Catterall WA. 2011. Voltage-gated calcium channels. *Cold Spring Harbor Perspect. Biol.* **3:** a003947.
3. Egenberger B, Polleichtner G, Wischmeyer E, Doring F. 2010. N-linked glycosylation determines cell surface expression of two-pore-domain K^+ channel TRESK. *Biochem. Biophys. Res. Commun.* **391:** 1262-1267.
4. Eklund EA, Freeze HH. 2006. The congenital disorders of glycosylation: a multifaceted group of syndromes. *NeuroRx* **3:** 254-263.
5. Fujita T, Utsunomiya I, Ren J, Matsushita Y, Kawai M, Sasaki S, *et al*. 2006. Glycosylation and cell surface expression of $K_v1.2$ potassium channel are regulated by determinants in the pore region. *Neurochem. Res.* **31:** 589-596.
6. Hall MK, Reutter W, Lindhorst T, Schwalbe RA. 2011. Biochemical engineering of the N-acyl side chain of sialic acids alters the kinetics of a glycosylated potassium channel $K_v3.1$. *FEBS Lett.* **585:** 3322-3327.
7. Hofmann F, Flockerzi V, Kahl S, Wegener JW. 2014. L-type $Ca_V1.2$ calcium channels: from *in vitro* findings to *in vivo* function. *Physiol. Rev.* **94:** 303-326.
8. Lee JH, Han DP. 2001. Expression of low voltage-activated Ca2+ channels in *Xenopus* oocytes. *J. Microbiol. Biotechnol.* **11:** 614-618.
9. Mikami A, Imoto K, Tanabe T, Niidome T, Mori Y, Takeshima H, *et al*. 1989. Primary structure and functional expression of the cardiac dihydropyridine-sensitive calcium channel. *Nature* **340:** 230-233.
10. Ohtsubo K, Marth JD. 2006. Glycosylation in cellular mechanisms of health and disease. *Cell* **126:** 855-867.
11. Orestes P, Osuru HP, McIntire WE, Jacus MO, Salajegheh R, Jagodic MM, *et al*. 2013. Reversal of neuropathic pain in diabetes by targeting glycosylation of $Ca_V3.2$ T-type calcium channels. *Diabetes* **62:** 3828-3838.
12. Perez-Reyes E. 2003. Molecular physiology of low-voltage-activated T-type calcium channels. *Physiol. Rev.* **83:** 117–161.
13. Schwetz TA, Norring SA, Bennett ES. 2010. N-glycans modulate $K_v1.5$ gating but have no effect on $K_v1.4$ gating. *Biochim. Biophys. Acta* **1798:** 367-375.
14. Scott H, Panin VM. 2014. The role of protein N-glycosylation in neural transmission. *Glycobiology* **24:** 407-417.
15. Splawski I, Timothy KW, Sharpe LM, Decher N, Kumar P, Bloise R, *et al*. 2004. $Ca_V1.2$ calcium channel dysfunction causes a multisystem disorder including arrhythmia and autism. *Cell* **119:** 19-31.
16. Weiss N, Black SA, Bladen C, Chen L, Zamponi GW. 2013. Surface expression and function of $Ca_v3.2$ T-type calcium channels are controlled by asparagine-linked glycosylation. *Pflugers Arch.* **465:** 1159-1170.
17. Wheeler DG, Groth RD, Ma H, Barrett CF, Owen SF, Safa P, Tsien RW. 2012. Ca_V1 and Ca_V2 channels engage distinct modes of Ca^{2+} signaling to control CREB-dependent gene expression. *Cell* **149:** 1112-1124.